LAWRENCE
LIVERMORE
NATIONAL
LABORATORY

LLNL-PROC-655976

Radiative Snowflake Divertor Studies in DIII-D.

V. A. Soukhanovskii

June 17, 2014

41st European Physical Society conference on Plasma Physics
Berlin, Germany
June 23, 2014 through June 27, 2014

Disclaimer

This document was prepared as an account of work sponsored by an agency of the United States government. Neither the United States government nor Lawrence Livermore National Security, LLC, nor any of their employees makes any warranty, expressed or implied, or assumes any legal liability or responsibility for the accuracy, completeness, or usefulness of any information, apparatus, product, or process disclosed, or represents that its use would not infringe privately owned rights. Reference herein to any specific commercial product, process, or service by trade name, trademark, manufacturer, or otherwise does not necessarily constitute or imply its endorsement, recommendation, or favoring by the United States government or Lawrence Livermore National Security, LLC. The views and opinions of authors expressed herein do not necessarily state or reflect those of the United States government or Lawrence Livermore National Security, LLC, and shall not be used for advertising or product endorsement purposes.

Radiative Snowflake Divertor Studies in DIII-D.

V.A. Soukhanovskii[1], S.L. Allen[1], M.E. Fenstermacher[1], D.N. Hill[1], C.J. Lasnier[1], M.A. Makowski[1], A.G. McLean[1], W.H. Meyer[1], E. Kolemen[2], R.J. Groebner[3], A.W. Hyatt[3], A.W. Leonard[3], T.H. Osborne[3], T.W. Petrie[3]

[1]*Lawrence Livermore National Laboratory, Livermore, CA, USA*
[2]*Princeton Plasma Physics Laboratory, Princeton, NJ, USA*
[3]*General Atomics, San Diego, CA, USA*

Introduction A snowflake divertor (SF) magnetic configuration [1] uses a second-order null created by merging two first-order nulls (X-points) of the standard divertor [1, 2]. Poloidal magnetic flux surfaces in the region of the exact second-order null have six hexagonal separatrix branches with an appearance of a snowflake, and the region of low poloidal field B_p surrounding the null(s) is broader (cf. standard divertor), leading to a strong impact on edge plasma properties. In the experiment, two variants of the exact configuration called snowflake-plus and snowflake-minus are often realized in steady-state, as the exact second-order null configuration is topologically unstable [1]. In the SF-plus, the secondary null is on the private flux region side of the standard divertor X-point. In the SF-minus, the secondary null approaches the standard divertor X-point from the common flux scrape-off layer (SOL) side (Fig. 1). Magnetic field structure and geometric properties of the SF-plus and the SF-minus are similar to those of the exact SF configuration when the distance D between the poloidal nulls satisfies $D \leq a\,(\lambda_q/a)^{1/3}$ (where a is the core minor radius and λ_q is the SOL power width (projected to midplane)) [2].

Experiments in DIII-D and NSTX at high divertor power density demonstrated significantly reduced inter-ELM divertor heat flux with both the SF-minus and the SF-plus, additional reduction with radiative dissipation, all compatible with high performance operation (H98y2$\geq$ 1) (e.g., [3, 4]). In this paper we discuss the impact of SF configurations on ELM energy and divertor heat transport and deposition. Type I ELM peak heat fluxes were significantly mitigated in the SF configurations, and nearly eliminated in D_2-seeded H-mode plasmas with $P_{NBI} = 4-5$ MW due to geometry, transport, and radiation effects.

Experiment The SF divertor configuration experiments were conducted in the DIII-D tokamak using a standard highly-shaped H-mode discharge scenario with $I_p = 1.2$ MA and $P_{NBI} = 4$ MW, and ion $B \times \nabla B$ direction toward the lower divertor. The DIII-D tokamak divertor is an open geometry divertor with graphite plasma-facing components and divertor inter-ELM heat fluxes of several MW/m^2. Radiative divertor conditions in DIII-D are routinely accessed with carbon and deuterium radiation using D_2 seeding that increases upstream (and core) density [5, 6]. The SF configurations were obtained for 2-3 s (cf. $\tau_E \sim 0.250$ s) using three existing poloidal field shaping coils in the divertor region.

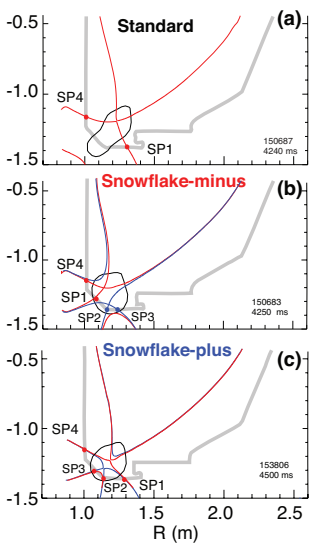

Figure 1: *Standard (a), SF-minus (b), and SF-plus (c) magnetic divertor configurations. The primary separatrix is shown by a red line, the secondary separatrix by blue lines.*

Impact on pedestal The SF configurations affected flux surface averaged edge magnetic properties via the poloidal magnetic field B_p, as a broader region of the low B_p (cf. standard X-point divertor) was formed inside the separatrix due to the two nulls in the lower divertor. Both the magnetic shear and q_{95} were systematically increased by 10-30%. Edge plasma profiles were similar with and without the SF configurations. Pedestal top plasma parameters varied within 5-15%: with the SF configuration, T_e^{ped} slightly reduced, n_e^{ped} slightly increased, and p_e^{ped} remained

nearly constant (Fig. 2). Changes in the magnetic shear and weak changes in pedestal pressure gradient were apparently insufficient to affect the peeling-balooning mode stability, as only small unsystematic changes in ELM frequency (about 10-20%) were detected with the SF. Pedestal energy W_{ped} was nearly unaffected at lower n_e. The pedestal stored energy lost per ELM ΔW_{ELM} was reduced in discharges with the SF configurations. In some discharges, the effect was strong, ΔW_{ELM} was reduced by up to 50% [4]. More typically, however, the reduction was in the range $\leq 20\%$. This was consistent with the Type I ELM scaling of ΔW_{ELM} with ν^*_{ped} found in many tokamaks [7]. In discharges with the SF divertor, the pedestal collisionality $\nu^*_{ped} = \pi R q_{95}/\lambda_{e,e}$ was increased and the ELM parallel transit time $\tau^{ELM}_{||} = 2\pi R q_{95}/c_{s,ped}$ (the pedestal ion transport time from the mid plane to the target at the sound speed c_s) was also increased. Shown in Fig. 2 are pedestal and ELM characteristics in the standard and the SF-minus divertor discharges at lower densities. At higher density in radiative SF divertor discharges, both the ΔW_{ELM} and $\Delta W_{ELM}/W_{ped}$ were lower by 10-20% (cf. standard divertor, Fig. 3).

The radiative SF discharges showed stronger reductions in ELM energies ΔW_{ELM}. Shown in Fig. 3 is a comparison of normalized ΔW_{ELM} for the lower n_e and radiative standard and SF-minus conditions. However, in these experiments the radiative divertor conditions were not optimized for compatibility with pedestal and core. While H-mode confinement was maintained, some reduction in $H98(y,2)$ by 10-20% with D_2 seeding was noted, mostly due to the reduction in pedestal T_e.

Impact on divertor The SF configurations also affected ELM heat transport in the SOL, resulting in reduced peak target temperatures and heat loads. Some uncertainties remain as to whether the SF configurations were maintained during equilibria perturbations due to large ELMs. Divertor infrared thermography data suggested that in many cases the SF configurations were not destroyed, and hence, the SF divertor geometry benefits were realized. These include increased connection length $L_{||}$, plasma-wetted area A_{wet}, specific divertor volume, and heat flux sharing among additional strike points.

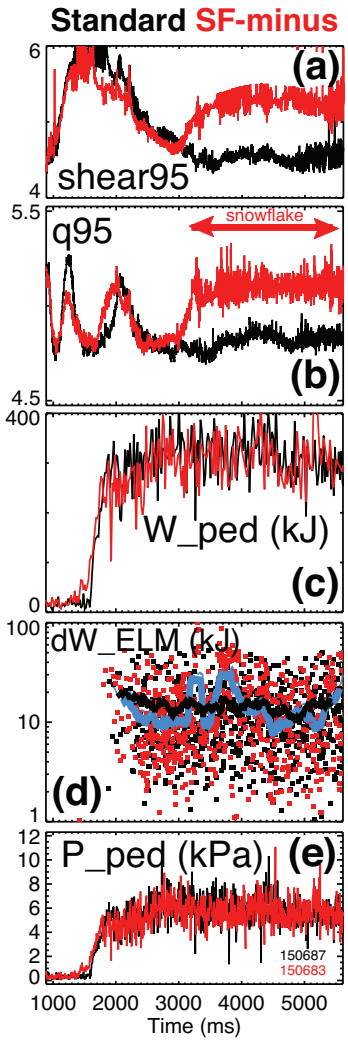

Figure 2: Time traces of edge magnetic shear (a), q_{95} (b), pedestal energy (c), energy lost per ELM (thick lines show average ΔW_{ELM}) (d), and pedestal pressure (e) in H-mode discharges with the standard and SF-minus divertors.

The peak divertor power was reduced in the SF-minus by up to 50-70%, and further reduced in the radiative SF-minus by up to 50%, as compared to the standard divertor. Shown in Fig. 3 is the divertor power operating space, the total power received by the outer (horizontal) target Q^{out}_{div} vs the power received by the inner (vertical) target Q^{in}_{div}, for the four discharges discussed above. The total power is obtained by integrating heat flux profiles measured by infrared thermography. Outer peak powers above 1-2 MW are attributed to ELMs in the standard and SF-minus at lower n_e. For ELMs, the increased divertor connection length $L_{||}$ reduces the target surface temperature rise as $\Delta T_t \sim W_{ELM}/\sqrt{\tau_d}$, where W_{ELM} is the ELM energy and τ_d is the ELM deposition time which is increased at longer $L_{||}$ [8]. The analysis of ELM plasma-wetted areas $A^{ELM}_{wet} = P^{ELM}_{div}/q^{ELM}_{peak}$, where P^{ELM}_{div} is the divertor power received during an ELM, showed no systematic trends in the outer divertor, and a reduced A^{ELM}_{wet} in the inner divertor in the SF configuration at lower n_e. Similar trends were observed at radiative conditions.

In the standard divertor configuration, radiative buffering of ELM divertor heat loads is not

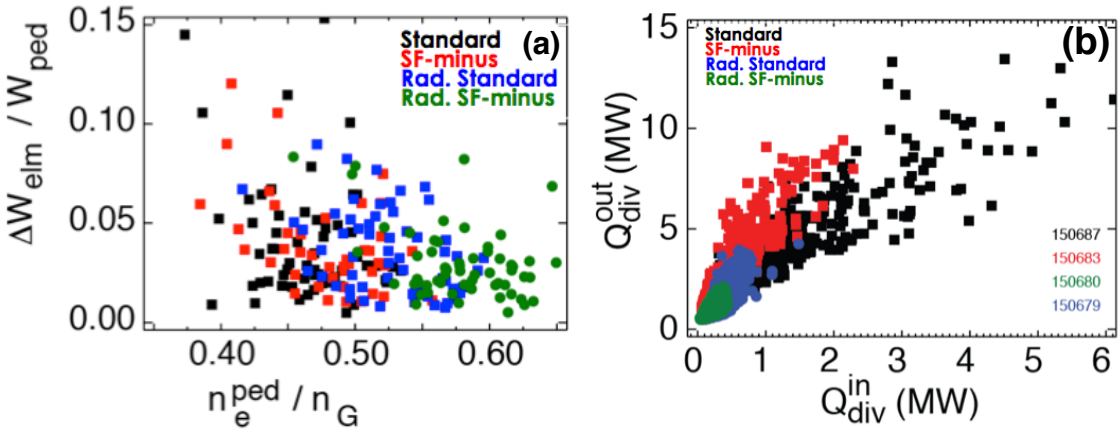

Figure 3: *(a) Energy lost per ELM reduction relative to the pedestal energy as a function of normalized pedestal density in the standard and SF-minus discharges at lower n_e and at higher n_e (radiative divertor conditions). (b) Divertor power operating space for the same conditions.*

very effective, leading to additional target power load reduction up to 20 % (e.g., [9]). Typically, the partially-detached standard divertor strike points re-attach during ELMs enabling significant transient heat and particle fluxes to reach the targets. Radiative SF divertor experiments in DIII-D demonstrated that at increased density (collisionality), both the ΔW_{ELM} and the divertor q_{peak}^{ELM} were reduced more strongly than in standard radiative divertor, leading to the much reduced peak powers. A combination of the geometry, transport and enhanced radiative dissipation may provide a significant benefit for ELM buffering. Shown in Fig. 4 are representative divertor heat flux profiles at peak ELM time in discharges with the SF-minus and standard divertors. At lower n_e, heat flows to all strike points in the SF divertor and q_{peak}^{ELM} is reduced, and nearly eliminated in the radiative SF, both in the inner strike point and the outer strike points. While the ELM power balance is not possible with present diagnostics, the Q_{div} operating space suggests that the reductions observed with the SF divertor must be due to the radiative dissipation and/or additional transport. We note that the radiative SF effect on ELM heat flux was also observed in the NSTX tokamak [10]

X-point β_p measurements The low B_p region in the SF configuration can affect transient heat transport not only via the geometry modifying the pedestal and SOL transport characteristics, but also via null-region ballooning, electrostatic, and flute-like instabilities [2, 11]. A toroidal curvature driven flute-like instability was conjectured to occur in the SF configuration [2, 12]. A convective redistribution of the ELM ion energy-carrying pulse among the additional separatrix branches would occur on a time scale much faster than the plasma travel time to the target plate. The low B_p region leads to a high $\beta_p = P_k/P_m = 8\pi P_k/B_p^2 \gg 1$, where $P_k = T_e n_e$ is the kinetic plasma pressure, and P_m is the poloidal magnetic plasma pressure. As the pressure balance condition no longer holds ($\beta_p \gg 1$), the poloidal equilibrium is not sustained and the plasma convectively mixes in the null-region $n = 0$ toroidally symmetric manifold, and spreads over all divertor legs.

The DIII-D unique diagnostic capability, the divertor Thomson scattering (DTS) diagnostic, was used to measure plasma kinetic pressure and infer β_p in the standard

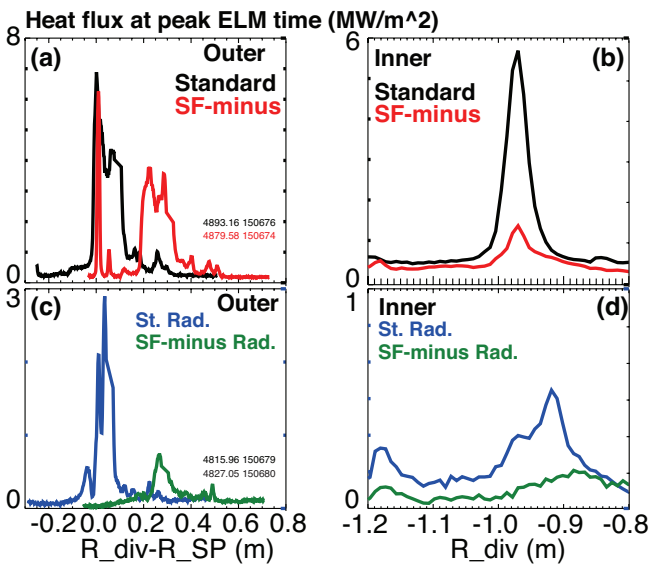

Figure 4: *Divertor heat flux profiles at peak ELM times.*

and SF null regions. While it is not presently possible to directly measure the mode frequency or amplitude, indirect measurements can aid modeling and theoretical calculations [2, 11, 12]. A special SF scenario was developed to position the null region over the DTS laser beam and sight lines (Fig. 5). The P_k profiles were obtained in the standard divertor configuration by slowly translating the X-point horizontally across the DTS region using the plasma control system. In the SF configuration, the translation capability was limited to a few cm. Most of the DTS data corresponds to the inter-ELM pressure, with a few incidentally synchronized ELMs. Shown in Fig. 5 is a comparison of the β_p profiles measured in the divertor X-point vicinity as a function of distance projected to midplane for the standard and SF-minus configuration. The SF data points are unsorted and correspond to several spatial locations above the divertor floor (indicated in the legend). First, β_p is low in the SOL, and rapidly approaches high values in the X-point vicinity. During ELMs, it increases by about an order of magnitude. Second, the region of high $\beta_p \geq 10-100$ is much broader in the SF configuration. For comparison, the measured midplane SOL separatrix $\beta_{pm} \leq 0.01$. Based on the theoretical estimates [2] and DIII-D parameters, we obtain for the size of the convective zone $D^* = a(\beta_{pm})^{1/4} \sim 20$ cm for the SF, and $D^* = a(\beta_{pm})^{1/2} \sim 6$ cm for the standard divertor.

In summary, recent DIII-D studies provide new insights into the physics of ELM energy loss, heat transport and deposition in the radiative SF divertor. The emerging understanding provides support to the SF divertor concept as a promising solution for divertor power exhaust in future magnetic fusion devices. The DIII-D experiments demonstrated the SF divertor compatibility with high H-mode confinement, radiative divertor with gas seeding, and significantly reduced ELM energies, as well as divertor heat fluxes between and during ELMs.

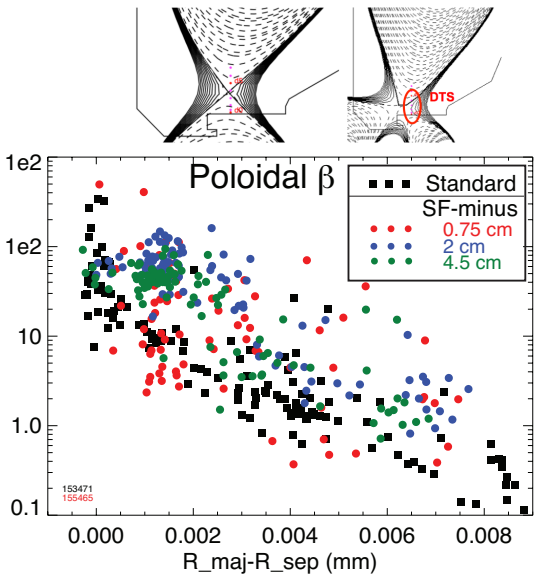

Figure 5: *Standard and SF-minus divertor configurations overlapping the DTS measurements region (top). Poloidal β_p measured in the divertor as a function of radial distance projected to the mid lane $R - R_{sep}$.*

Acknowledgements We thank the entire DIII-D Team for technical, engineering and computer support as well as plasma and diagnostic operations. Dr. D. D. Ryutov is acknowledged for insightful discussions. This work was performed under the auspices of the US Department of Energy (US DOE) under DE-AC52-07NA27344, DE-AC02-09CH11466, DE-FC02-04ER54698 and DE-AC04-94AL85000.

References

[1] RYUTOV, D., Phys. Plasmas **14** (2007) 064502.
[2] RYUTOV, D. et al., Plasma Physics and Controlled Fusion **54** (2012).
[3] SOUKHANOVSKII, V. et al., Phys. Plasmas **19** (2012/08/) 082504 (12 pp.) .
[4] HILL, D., Nucl. Fusion **53** (2013/10/) 104001 (18 pp.) .
[5] PETRIE, T. et al., Nuclear Fusion **37** (1997) 321 .
[6] FENSTERMACHER, M. E. et al., Plasma Phys. Control. Fusion **41** (1999) A345.
[7] LOARTE, A. et al., Journal of Nuclear Materials **313–316** (2003) 962 .
[8] ROGNLIEN, T. et al., Journal of Nuclear Materials **438** (2013) S418 .
[9] MONIER-GARBET, P. et al., Nuclear Fusion **45** (2005) 1404.
[10] SOUKHANOVSKII, V. et al., Journal of Nuclear Materials **438** (2013) S96 .
[11] RYUTOV, D. et al., in *Proc. 24th IAEA FEC, San Diego, 2012*, Paper TH/P4-18.
[12] RYUTOV, D. et al., Phys. Scripta **accepted** (2014).